[2] K. Everszumrode, B. Brockmann, and D. Jäger, "Über den Wirkungsgrad der Frequenzvervielfachung längs Schottky-Kontakt-Leitungen," in preparation.
[3] D. Jäger and W. Rabus, "Bias-dependent phase delay of Schottky contact microstrip line," *Electron. Lett.*, vol. 9, pp. 201–202, May 1973.
[4] D. Jäger, W. Rabus, and W. Eickhoff, "Bias-dependent small-signal parameters of Schottky contact microstrip lines," *Solid-St. Electron.*, vol. 17, pp. 777–783, Aug. 1974.
[5] D. Jäger, "Wellenausbreitung auf Schottky-Kontakt-Leitungen im Kleinsignalbetrieb," thesis, University of Münster, Germany, 1974.
[6] W. Schäfer, J. P. Becker, and D. Jäger, "Variable Tiefpassfilter in Streifenleitungstechnik," in preparation.
[7] D. Jäger and W. Rabus, "Elektrische Leitung auf halbleitendem Substratmaterial," patent pending, 1973.
[8] H. Guckel, P. A. Brennan, and I. Palocz, "A parallel-plate waveguide approach to microminiaturized planar transmission lines for integrated circuits," *IEEE Trans. Microwave Theory Tech.*, vol. MTT-15, pp. 468–476, Aug. 1967.
[9] I. T. Ho and S. K. Mullick, "Analysis of transmission lines on integrated circuit chips," *IEEE J. Solid-St. Circuits*, vol. SC-2, pp. 201–208, Dec. 1967.
[10] H. Hasegawa and H. Yanai, "Characteristics of parallel-plate waveguide filled with a silicon-siliconoxide system," *Electron. and Commun. Jap.*, vol. 53-B, no. 10, pp. 63–73, 1970.
[11] H. Hasegawa, M. Furukawa, and H. Yanai, "Properties of microstrip line on Si–SiO_2 system," *IEEE Trans. Microwave Theory Tech.*, vol. MTT-19, pp. 869–881, Nov. 1971.
[12] J. M. Jaffe, "A high frequency variable delay line," *IEEE Trans. Electron Devices*, vol. ED-19, pp. 1292–1294, Dec. 1972.
[13] U. Günther and E. Voges, "Variable capacitance MIS microstrip lines," *AEÜ*, vol. 27, pp. 131–139, March 1973.
[14] S. M. Sze, *Physics of Semiconductor Devices*. New York: Wiley-Interscience, 1969.
[15] R. E. Collin, *Field Theory of Guided Waves*. New York: McGraw-Hill, 1960.
[16] a) R. A. Pucel, D. J. Masse, and C. P. Hartwig, "Losses in microstrip," *IEEE Trans. Microwave Theory Tech.*, vol. MTT-16, pp. 342–350, June 1968.
b) ——, "Correction to 'Losses in microstrip'," *ibid.* (Corresp.), vol. MTT-16, p. 1064, Dec. 1968.

Analysis of a Waveguide Mounting Configuration for Electronically Tuned Transferred-Electron-Device Oscillators and its Circuit Application

J. S. JOSHI AND J. A. F. CORNICK

Abstract—**Theoretical analysis of a waveguide-post mounting configuration employed for high electronic (varactor) tuning of a transferred-electron-device oscillator is presented. The resulting two-port-coupling network representation is also used to derive the impedance of the post structure as an obstacle to the dominant TE_{10} mode in the waveguide. Obstacle measurements conducted on the post structure for the incident TE_{10} mode are found to be in very good agreement with the theory.**

This network representation is then applied to a practical transferred-electron-device oscillator reported elsewhere. It has been able to successfully explain the characteristic features of the oscillator. It is observed that the main source of discrepancy between the theoretical and experimental characteristics could be attributed to a lack of knowledge of the precise values of the package parasitic elements. The nature of the theoretical varactor-tuning characteristic predicted by the model is discussed and indicated for a particular configuration.

Introduction

ELECTRONICALLY TUNED transferred-electron oscillators are finding increasing practical applications. There are mainly two elements which can be used for electronic tuning of transferred-electron-device oscillators, namely YIG elements and varactor diodes. Although YIG-tuned transferred-electron oscillators are capable of providing a large electronic tuning range [1] (of the order of an octave), they are not favored in most systems applications because of their sluggish dynamic response. Varactor diodes, on the other hand, have a very fast dynamic response and are therefore more frequently used in the systems demanding fast response rates.

However, for good noise performance, it is also desirable that such varactor-tuned transferred-electron-device oscillators be constructed in relatively high-Q configurations. Standard-height waveguide cavities provide such configurations. The first published results on a varactor-tuned transferred-electron oscillator in a full-height waveguide cavity [2] reported an electronic tuning range of over 1 GHz in X band. This configuration utilized post mounting arrangements in which the transferred-electron device and the varactor diode were mounted on separate posts at the opposite ends of the waveguide height. The posts were located as close as is mechanically possible to maximize the degree of coupling between the two devices. In the limiting case when the two posts merge, that is, when the devices are located at the opposite ends of the same post, one would expect an even greater electronic tuning range. Such a configuration [Fig. 1(a)] has been utilized to obtain large electronic tuning ranges [3], [4].

It is the aim of this paper to characterize such mounting configurations in the form of a multiport network. This network will be used to explain the experimentally observed results [4].

Manuscript received April 30, 1975; revised March 15, 1976.
The authors are with Mullard Hazel Grove Ltd., Bramhall Moor Lane, Hazel Grove, Cheshire SK7 5BJ, England.

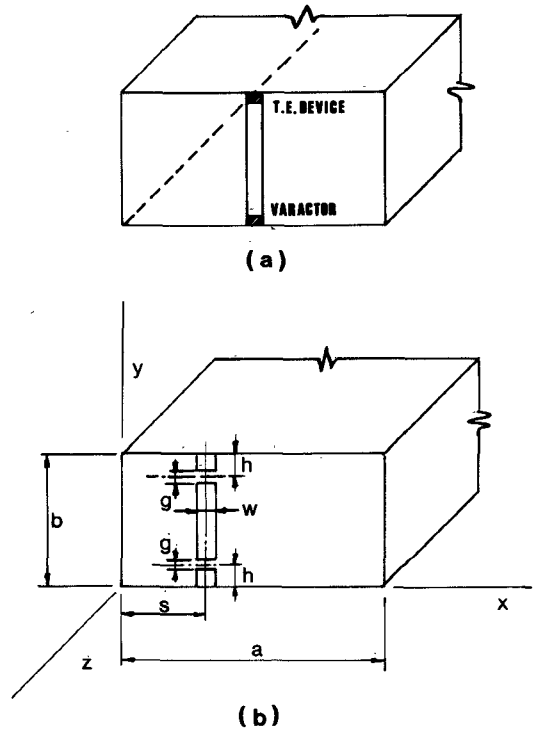

Fig. 1. Mounting configuration (a) for electronically tuned transferred-electron-device oscillator; (b) parameter definition for the general configuration.

Analysis of the Mounting Configuration

Here the approach taken by Eisenhart and Khan [5] for single-post single-gap configuration is extended to the single-post two-gap symmetrical configuration of Fig. 1(b). Following [5] the post is replaced by a strip of width $w = 1.8d$, where d is the post diameter. It is assumed that the introduction of another gap does not alter the assumption of uniform current density across the strip and uniform electric-field distribution in the gaps [5]. These assumptions, however, can only be verified by conducting actual measurements on the post geometry. The analysis adopts the technique of symmetrical and antimetrical excitation used by El-Sayed [6].

Dyadic Green's Function

For a rectangular waveguide this is given by

$$\boldsymbol{G}(r/r') = \hat{y}\hat{y} \sum_{n=0}^{\infty} \sum_{m=1}^{\infty} \frac{(2-\delta_n)(k^2 - k_y^2) \exp(-\Gamma_{mn}|z-z'|)}{abk^2\Gamma_{mn}} \cdot \sin k_x x \sin k_x x' \cos k_y y \cos k_y y' \tag{1}$$

where

$$k_x = m\pi/a; \quad k_y = n\pi/b; \quad k = 2\pi/\lambda$$

$$\Gamma_{mn} = (k_x^2 + k_y^2 - k^2)^{1/2}$$

$$\delta_n = 1, \quad \text{for } n = 0$$
$$= 0, \quad \text{for } n \neq 0.$$

Current-Density Distribution

Following [5] the current-density distribution $\boldsymbol{J}(r)$ can be expressed as

$$\boldsymbol{J}(r) = \hat{y} J_0 u(x) u(y) \delta(z-0) \tag{2}$$

with

$$u(x) = \sum_{f=1}^{\infty} \frac{(2-\delta_f)}{a} [A_f^x \cos(f\pi x/a) + B_f^x \sin(f\pi x/a)]$$

$$u(y) = \sum_{1=0}^{\infty} \frac{(2-\delta_1)}{b} [A_1^y \cos(1\pi y/b) + B_1^y \sin(1\pi y/b)] \tag{3}$$

$$\delta(z-0) = 1, \quad \text{for } z = 0$$
$$= 0, \quad \text{elsewhere.}$$

The current-density distribution is assumed to be constant across the width of the strip w, and the normalizing coefficients A_f^x and B_f^x can be expressed as

$$A_f^x = w \cos\frac{f\pi s}{a} \frac{\sin\theta_f}{\theta_f}$$

$$B_f^x = w \sin\frac{f\pi s}{a} \frac{\sin\theta_f}{\theta_f} \tag{4}$$

where $\theta_f = f\pi w/2a$.

Electric-Field Distribution $\boldsymbol{E}(r)$

It is given by

$$\boldsymbol{E}(r) = -j\omega\mu \int_V \boldsymbol{G}(r \mid r') \cdot \boldsymbol{J}(r')\, dV$$

$$= -\hat{y} \frac{j\eta J_0}{abk} \sum_{n=0}^{\infty} \sum_{m=1}^{\infty} \frac{(2-\delta_n)(k^2 - k_y^2) \exp(-\Gamma_{mn}|z|)}{\Gamma_{mn}} \cdot A_n^y B_m^x \sin k_x x \cos k_y y. \tag{5}$$

The Gap Electric Fields

The two gaps in general will be driven by voltages V_1 and V_2, respectively. This general excitation can be reduced to a linear combination of symmetrical and antimetrical excitation, denoted by superscripts s and a, respectively. This results in

$$\boldsymbol{E}_g^s = -\hat{y} \frac{V^s}{g} v(x) v^s(y) \delta(z-0) \tag{6}$$

$$\boldsymbol{E}_g^a = -\hat{y} \frac{V^a}{g} v(x) v^a(y) \delta(z-0) \tag{7}$$

where

$$V^s = \frac{V_1 + V_2}{2}$$

$$V^a = \frac{V_1 - V_2}{2}$$

$$v(x) = 1, \quad \text{for } s - \frac{w}{2} \leq x \leq s + \frac{w}{2}$$
$$= 0, \quad \text{elsewhere}$$

$$v^s(y) = \sum_{p=0}^{\infty} \frac{(2-\delta_p)}{b} S_p^{y,s} \cos(p\pi y/b) \tag{8}$$

$$v^a(y) = \sum_{p=0}^{\infty} \frac{(2-\delta_p)}{b} S_p^{y,a} \cos(p\pi y/b). \tag{9}$$

The y-distribution functions $v^s(y)$ and $v^a(y)$ can be specifically defined as

$$\begin{aligned} v^s(y) &= \tfrac{1}{2}, && \text{for } h - g/2 \le y \le h + g/2 \\ &= -\tfrac{1}{2}, && \text{for } b - h - g/2 \le y \le b - h + g/2 \\ &= 0, && \text{elsewhere} \end{aligned} \tag{10}$$

$$\begin{aligned} v^a(y) &= \tfrac{1}{2}, && \text{for } h - g/2 \le y \le h + g/2 \\ &= \tfrac{1}{2}, && \text{for } b - h - g/2 \le y \le b - h + g/2 \\ &= 0, && \text{elsewhere} \end{aligned} \tag{11}$$

resulting in

$$\begin{aligned} S_p^{y,s} &= g \cos \frac{p\pi h}{b} \frac{\sin \phi_p}{\phi_p}, && \text{for } n \text{ odd} \\ &= 0, && \text{for } n \text{ even} \end{aligned} \tag{12}$$

$$\begin{aligned} S_p^{y,a} &= g \cos \frac{p\pi h}{b} \frac{\sin \phi_p}{\phi_p}, && \text{for } n \text{ even} \\ &= 0, && \text{for } n \text{ odd} \end{aligned} \tag{13}$$

where $\phi_p = p\pi g/2b$.

Space-Harmonic Functions and Impedance Relationships

The total power incident on both gaps for symmetrical and antimetrical excitation for the nth spatial-harmonic mode is given by $2 \int \boldsymbol{E}_g^s \cdot \boldsymbol{J}\, dV$ and $2 \int \boldsymbol{E}_g^a \cdot \boldsymbol{J}\, dV$, respectively. This incident power must be equal to the power radiated throughout the volume for both symmetrical and antimetrical excitation, respectively.

Now

$$\begin{aligned} 2 \int \boldsymbol{E}_g^s \cdot \boldsymbol{J}\, dV &= -2V^s J_0 w \sum_{\substack{n=1,3,5\cdots \\ \text{odd}}}^{\infty} \frac{(2 - \delta_n)}{b} A_n^y \cos k_y h \frac{\sin \phi_n}{\phi_n} \\ &= 0, \quad \text{for } n \text{ even.} \end{aligned} \tag{14}$$

Similarly,

$$\begin{aligned} 2 \int \boldsymbol{E}_g^a \cdot \boldsymbol{J}\, dV &= -2V^a J_0 w \sum_{\substack{n=0,2,4 \\ \text{even}}}^{\infty} \frac{(2 - \delta_n)}{b} A_n^y \cos k_y h \frac{\sin \phi_n}{\phi_n} \\ &= 0, \quad \text{for } n \text{ odd.} \end{aligned} \tag{15}$$

Resulting in

$$\begin{aligned} I_n^s &\equiv \frac{(2 - \delta_n)}{b} A_n^y J_0 w \cos k_y h \frac{\sin \phi_n}{\phi_n}, && \text{for } n \text{ odd} \\ &\equiv 0, && \text{for } n \text{ even} \end{aligned} \tag{16}$$

and

$$\begin{aligned} I_n^a &\equiv \frac{(2 - \delta_n)}{b} A_n^y J_0 w \cos k_y h \frac{\sin \phi_n}{\phi_n}, && \text{for } n \text{ even} \\ &\equiv 0, && \text{for } n \text{ odd.} \end{aligned} \tag{17}$$

Also $I_n = I_n^s + I_n^a$. The radiated power throughout the volume for each nth spatial-harmonic mode is given by

$$P_n = \int_V \boldsymbol{E} \cdot \boldsymbol{J}\, dV, \qquad \text{for } n = 0,1,2,3,\cdots,\infty$$

$$P_n = -\frac{j\eta J_0^2 w^2 (2 - \delta_n)(k^2 - k_y^2)(A_n^y)^2}{abk} \cdot \sum_{m=1}^{\infty} \frac{\sin^2 k_x s}{\Gamma_{mn}} \left(\frac{\sin \theta_m}{\theta_m}\right)^2, \qquad \text{for } n = 0,1,2,3,\cdots,\infty. \tag{18}$$

This should be equal, separately, to the power incident on the gaps, that is,

$$2V^s I_n^s = P_n$$

$$2V^a I_n^a = P_n.$$

Since the gap driving-point impedance is given by $Z_n = V/I_n$ for each nth spatial harmonic, this results in

$$\begin{aligned} Z_n^s = 1/Y_n^s &= j\eta \frac{b}{2a} \frac{(k^2 - k_y^2)}{(2 - \delta_n)k} \sum_{m=1}^{\infty} \frac{(k_{pm}/k_{gn})^2}{\Gamma_{mn}}, && \text{for } n \text{ odd} \\ &= \infty, && \text{for } n \text{ even} \end{aligned} \tag{19}$$

$$\begin{aligned} Z_n^a = 1/Y_n^a &= j\eta \frac{b}{2a} \frac{(k^2 - k_y^2)}{(2 - \delta_n)k} \sum_{m=1}^{\infty} \frac{(k_{pm}/k_{gn})^2}{\Gamma_{mn}}, && \text{for } n \text{ even} \\ &= \infty, && \text{for } n \text{ odd} \end{aligned} \tag{20}$$

where

$$k_{pm} = \sin k_x s \frac{\sin \theta_m}{\theta_m}$$

$$k_{gn} = \cos k_y h \frac{\sin \phi_n}{\phi_n}. \tag{21}$$

For each nth spatial harmonic there exists a coupling network between the two gaps. The complete equivalent network is therefore composed of an infinite number of such coupling networks for $n = 0,1,2,\cdots,\infty$, connected in parallel between the two gap ports as shown in Fig. 2(a). Each individual network can be represented in the form of either a T or a π network whose elements are related to the symmetrical and antimetrical immittances of (19) and (20).

The two-port network representation for this configuration for each spatial-harmonic mode appears to be in conflict with that suggested by simple physical reasoning; according to which the two gap ports should be directly coupled in

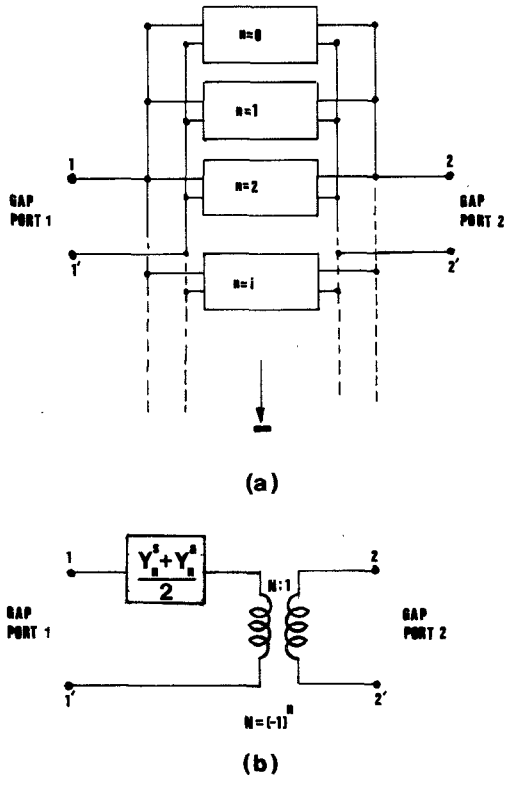

Fig. 2. (a) Total coupling network between the two gap ports as a parallel combination of individual networks corresponding to each spatial harmonic. (b) Alternative representation of an individual coupling network.

series. However, if an alternative admittance coupling network representation [7] is used; then since for each spatial harmonic the determinant of the admittance matrix is zero, the coupling network reduces to the simple physically expected form of Fig. 2(b). It should, however, be noted that although the two gap ports are connected in series, for each odd value of n there is phase reversal between the two gap ports. In other words, the dot convention on the transformer changes for every alternate value of n.

Obstacle Representation

Following the approach taken in [6], the obstacle circuit for the incident TE_{10} mode can be derived as shown in Fig. 3. The element values are given by

$$jX_L' = \sum_{m=2}^{\infty} Z_{m0} \cdot k_{pm}^2/2 \tag{22}$$

$$Y_A = \frac{1}{Z_A} = \sum_{n=1}^{\infty} \left[\sum_{m=1}^{\infty} \frac{Z_{mn}}{2} \cdot \left(\frac{k_{pm}}{k_{gn}}\right)^2 \right]^{-1}, \quad \text{for } n \text{ odd}$$

$$= 0, \quad \text{for } n \text{ even} \tag{23}$$

$$Y_B = \frac{1}{2_B} = \sum_{n=1}^{\infty} (-1)^n \left[\sum_{m=1}^{\infty} Z_{mn}(k_{pm}/k_{gn})^2 \right]^{-1}, \quad \text{for all } n \tag{24}$$

where

$$Z_{mn} = j\eta \frac{b}{a} \frac{k^2 - k_y^2}{(2 - \delta_n)k} \cdot \frac{1}{\Gamma_{mn}}.$$

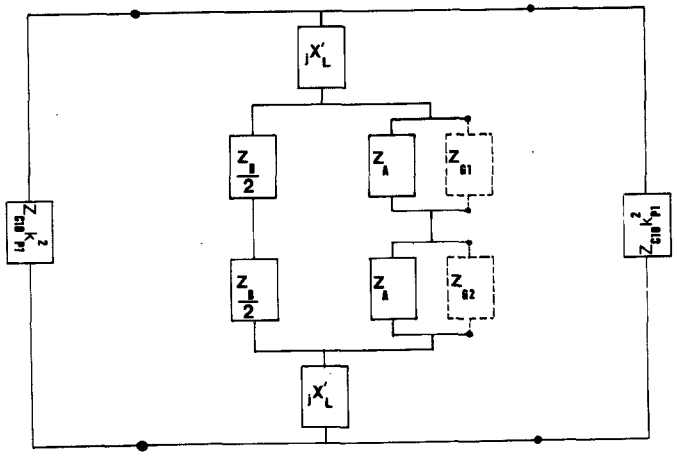

Fig. 3. Representation of the obstacle as a shunt impedance for incident TE_{10} mode.

For symmetrical gap loading $Z_{G1} = Z_{G2} = Z_G = 1/Y_G$ the obstacle impedance is given by

$$Z_{obs} = \frac{2}{k_{p1}^2} \left[jX_L' + \frac{1}{Y_A + 2Y_B + Y_G} \right]. \tag{25}$$

A comparison with the obstacle representation of [5] shows that the element value jX_L' corresponds to one-half the flat post reactance of the post configuration. The modified gap driving-point admittance Y_R' is replaced here by admittances Y_A for each gap and the two gaps are coupled by the coupling admittance Y_B.

The convergence properties of these element values are similar to those discussed by El-Sayed [6]. Following [5] in the computational work the upper limit for summation is $2M_1$ in (22) with a correction factor $(1 - w/a)$ for deviations from the assumed current-density distribution. The upper limits for summation of m and n in (23) and (24) are $M_1 = a/w$ and $N_1 = b/g$, respectively. These limits and correction factor are utilized throughout for both the experimental work and circuit application studies reported here. Also $w = 1.8d$ is used throughout the work.

Experimental Measurements

The two-port-coupling network representation derived in the previous section can be verified by conducting measurements on the two gap ports of the mounting configuration along the lines adopted by Eisenhart and Khan [5]. In [5], even though only a one-port network was being considered, the driving-point impedance could not be easily measured. Here the two-port symmetrical network necessitates at least two-measurements at one gap port while the other is terminated in precisely known impedances making the task even more difficult.

Although this technique provides a direct verification of the proposed equivalent circuit, its implementation into practically realizable objects is quite difficult. The fact that two gaps will have to be located on the same post structure and one of the gap ports will have to be terminated in accurately known impedances, makes the mechanical arrangement of the experimental mount extremely complex and difficult to fabricate. Moreover, the lack of commercially available ultraminiature coaxial connectors requires that

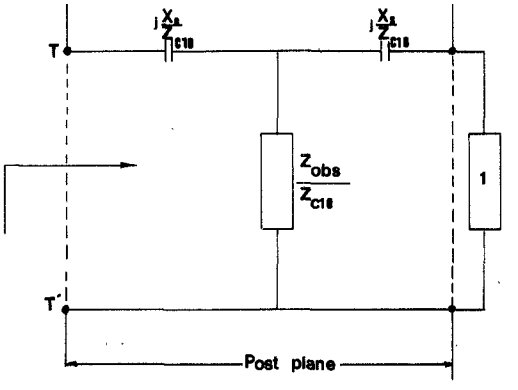

(a)

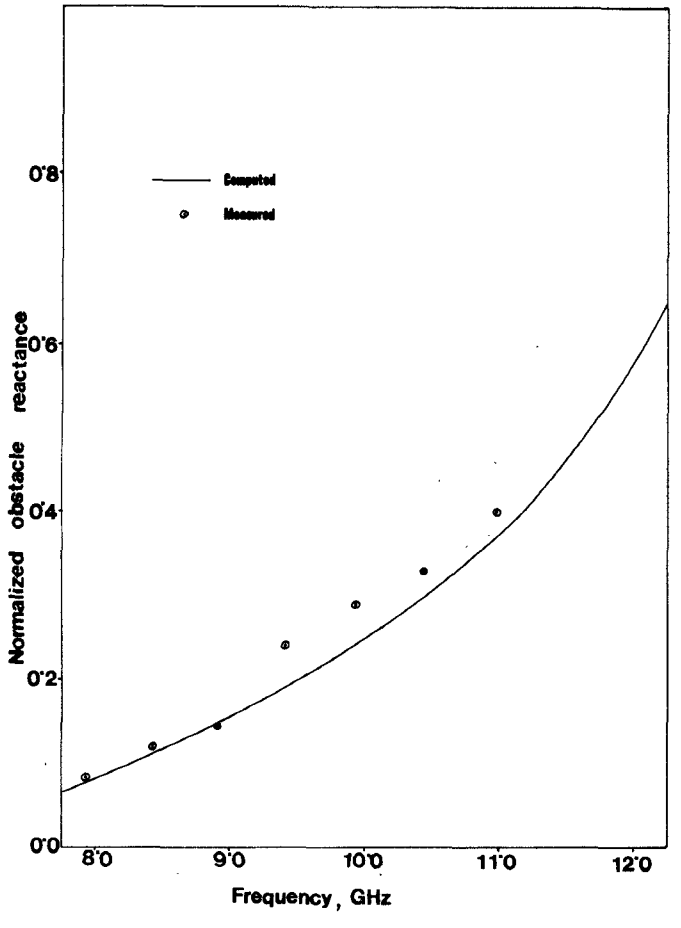

(b)

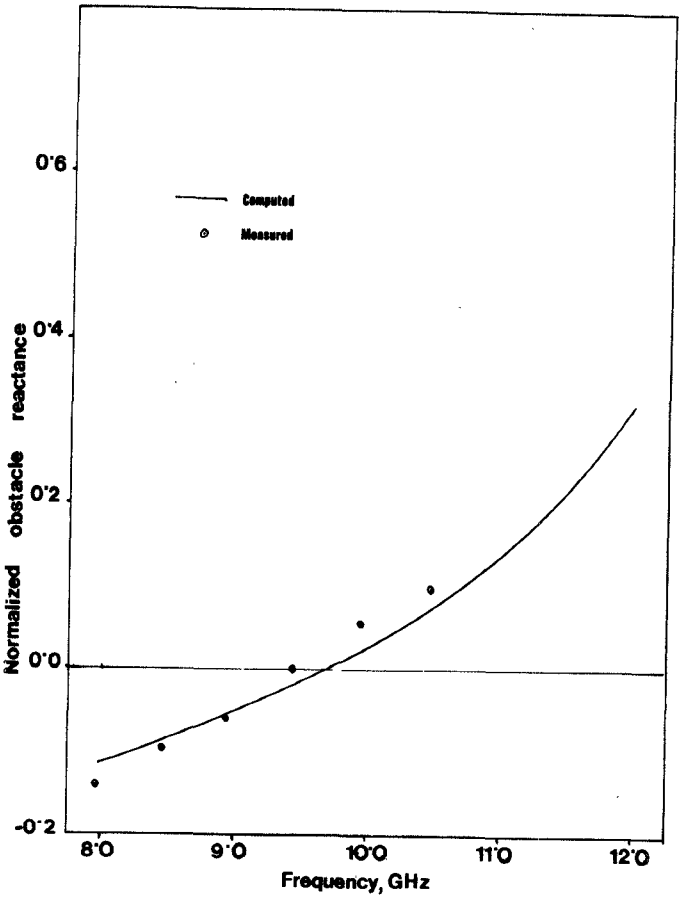

(c)

Fig. 4. (a) Equivalent circuit for measurement of obstacle shunt impedance. (b) Measured and computed values of normalized obstacle shunt reactance. Parameter values are $a = 22.86$ mm; $b = 10.16$ mm; $s = 15.3$ mm; $d = 2.3$ mm; $h = 2.525$ mm; and $g = 0.63$ mm. The gaps are symmetrically loaded and contain 2.3-mm-diam circular alumina disks (dielectric constant = 10). (c) Measured and computed values of normalized obstacle shunt reactance. Parameter values are $a = 22.86$ mm; $b = 10.16$ mm; $s = 7.5$ mm; $d = 2.9$ mm; $h = 3.15$ mm; and $g = 0.63$ mm. The gaps are unsymmetrically loaded; one gap contains 2.3-mm-diam circular alumina disk (dielectric constant = 10), the other is an air gap.

measurements be carried out in larger cross-section waveguides like S or C band.

The alternative technique of measuring obstacle shunt impedance which was adopted both by Eisenhart and Khan [5] and El-Sayed [6] has been followed here for the verification of the theoretical model. It is a simple and convenient means to that end.

The measurements were conducted in X band using slotted-line techniques. One of the waveguide ports was match terminated and impedance measured at the other port. The total obstacle network is shown in Fig. 4(a) in which the effect of the finite post diameter is accounted for by the reactance jX_s [7]. The experimental value of normalized obstacle shunt impedance is arrived at from the measured values of the normalized impedance at the $T - T'$ plane and the normalized phase-shift reactance.

Two different post configurations were fabricated, both with off-center post axis locations. The gap terminations on the first configuration were symmetrical in the form of circular alumina pieces 0.025 in thick. In the second configuration one of the gaps was partially filled with a 0.025-in-thick circular alumina piece while the second one was an air gap, thus providing an unsymmetrically loaded obstacle. The gap-terminating impedance in each case was taken to be that due to the appropriate parallel-plate capacitance. Fringing effects were not included.

Theoretical and experimental obstacle impedance values for the two configurations are shown in Fig. 4(b) and (c). It can be seen that a good correlation has been obtained. It is interesting to note that in Fig. 4(b) the obstacle reactance is always inductive while in Fig. 4(c) it changes from capacitive to inductive.

It can be seen from Fig. 3 and (23) and (24) that the elements Y_A and Y_B which are part of the total obstacle shunt impedance, are capacitive and inductive, respectively. The gap-terminating impedances for the cases considered here are capacitive. Thus the element Y_B and the combination of elements Y_{G1}, Y_{G2}, and Y_A form a parallel resonant circuit. For the case shown in Fig. 4(c), because one of the gap-terminating admittances is small (air gap), the impedance of the parallel resonant circuit is capacitive for the lower frequency region and large enough to overcome the series inductive reactance term $j2X_L'$, thus providing a capacitive obstacle shunt impedance. For the case shown in Fig. 4(b), both the gaps are dielectrically loaded and the gap-terminating admittance is large. The resonant frequency of the parallel resonant circuit is therefore lower and in the frequency range of interest the obstacle shunt impedance is always inductive.

It should, however, be pointed out that the theoretical model does not take various losses involved in the system into account. This would explain the discrepancy between the measured and theoretical values of obstacle shunt impedance for the upper frequency regions. These experimental results, however, do provide a verification of the theoretical model and a basis for using this model for circuit-application studies.

Circuit Application

Having verified the general equivalent network for a symmetrical two-gap single-post configuration, it will be applied to a practical arrangement utilized by Dean and Howes [3], [4] for obtaining large varactor-tuning ranges in the K_u-band frequency region.

The mounting arrangement utilized in [3], [4] is similar to that shown in Fig. 1(a) with a sliding short-circuit termination on one side and a matched output. L represents the distance between the device plane and the short-circuit plane. Dean and Howes [4] had proposed a rather simplified equivalent-circuit representation for the configuration. The two gap ports were directly coupled by an inductive element, corresponding to the full post reactance expression of Marcuvitz [7]. It is worthwhile noting here that this expression does not take into account $n > 0$ terms for m, n modes [7].

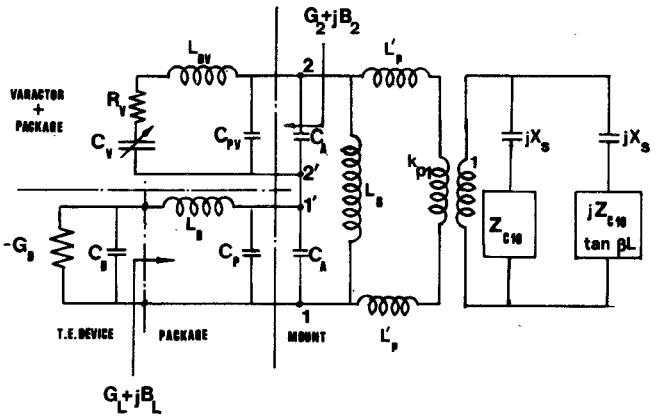

Fig. 5. Equivalent-circuit representation for the mounting configuration of Fig. 1(a) with short-circuit termination on one side. Mounting configuration parameters are: $a = 15.8$ mm; $b = 7.9$ mm; $s = 7.9$ mm; $d = 2.54$ mm; $h = 0.8$ mm; and $g = 1.6$ mm. Parameter values for devices are as indicated in [4], that is: Varactor diode: $R_V = 1\ \Omega$, $C_V(0) = 0.95$ pF, $C_V(30) = 0.2$ pF, $L_{DV} = 0.9$ nH, $C_{PV} = 0.19$ pF. T.E. device: Maximum device conductance $= -5$ mS, $C_D = 0.27$ pF, $L_D = 0.6$ nH, $C_p = 0.17$ pF.

The proposed equivalent circuit based on a general two-port coupling network is shown in Fig. 5. This network is valid for the dominant TE_{10}-mode frequency range and is derived from the obstacle representation of Fig. 3. The post-thickness capacitive reactance term jX_s [7] has also been included. The self-admittance term Y_A of the two gap ports is replaced by its equivalent capacitance C_A, which accounts for the total capacitive effect of all TE_{mn} and TM_{mn} modes for all odd values of n. The mutual admittance term Y_B is replaced by its equivalent inductance L_B, which accounts for the total inductive effect of all TE_{mn} and TM_{mn} modes for all values of n. The one-half flat post reactance jX_L' (for TE_{m0}, $m > 1$) of the mounting post is represented by its equivalent inductance L_p'. The terminations on the waveguide ports are represented by Z_{c10} (characteristic impedance for TE_{10} mode) and $jZ_{c10} \tan \beta L$ (effect of short circuit).

Package equivalent circuits of the transferred-electron device and varactor diode and their parameter values are as indicated by Dean and Howes [4]. The maximum transferred-electron-device conductance of -5 mS is consistent with the kind of device used [3], [4] and other parameter values. Standard WG18 waveguide cavity configuration with 1.6-mm gap size (for S4 package) is used in the theoretical model. The post diameter in Dean and Howes [4] work was 2.54 mm. With this value the current-density distribution in the post and electric-field distribution in the gap may slightly deviate from the assumed uniform distribution. Eisenhart and Khan [8] have, however, successfully used their model to predict experimental results under identical conditions.

Oscillation Conditions and Stability Criteria

For sustained circuit-controlled steady-state oscillations it is necessary to satisfy the conditions

$$G_D(\omega) + G_L(\omega) = 0 \tag{26}$$

$$B_D(\omega) + B_L(\omega) = 0 \tag{27}$$

where $G_D(\omega)$ and $B_D(\omega)$ are, respectively, real and imaginary parts of the device admittance, and $G_L(\omega)$ and $B_L(\omega)$ are, respectively, real and imaginary parts of the load admittance.

Besides these steady-state oscillation conditions the stability condition should also be satisfied [9], which is

$$\frac{\partial B(\omega)}{\partial \omega} > 0 \tag{28}$$

where $B(\omega)$ is the total susceptance $B_D(\omega) + B_L(\omega)$ of the circuit. Kurokawa's [10] work also provides the same stability criteria, which are derived under the assumption that the negative resistance (or conductance) of the device be frequency independent, which is clearly not the case for transferred-electron devices.

Many workers when dealing with transferred-electron oscillators utilize the criteria of (28) for locating stable operating points and determining the mode-switching points [11]–[13]. These criteria generally render excellent agreement between theory and experiment.

Eisenhart and Khan [8], however, use two postulates for deciding upon the stable operating points. The postulates are: 1) The output power of the negative-conductance device increases with the load conductance G_L, for $G_L \leq |G_D|$, with maximum output power as $G_L \rightarrow |G_D|$, where $|G_D|$ is the maximum value of conductance the device can deliver [not to be confused with $G_D(\omega)$ of (26)]; and 2) under multiresonant-circuit conditions the oscillation will occur at the frequency for which G_L is maximum, though not greater than $|G_D|$. Using these two postulates the theoretical tuning characteristics of the oscillator can be determined at a glance.

It should, however, be noted that the model ignores the effect of variation of transferred-electron-device parameters $G_D(\omega)$ and $C_D(\omega)$ with RF power and frequency. It also ignores the changes in the varactor diode series resistance and junction capacitance at zero bias, which under some conditions may become forward biased due to a large amount of incident RF power.

Tuning Characteristics

Fig. 6(a) shows the tuning characteristics of the oscillator at zero varactor bias corresponding to $C_V = 0.95$ pF. The switching points are determined by using the second postulate of Eisenhart and Khan [8] and the stability criteria of (28). Fig. 6(b) contains the load and device susceptance variation with frequency for different short-circuit locations. Load conductance values at each oscillation point and their stable or unstable modes of operation are indicated. In Fig. 6(a), according to Eisenhart and Khan's [8] second postulate, the oscillation points for which $G_L = 0.26$, 0.97, and 3.06 are unstable. However, according to the stability criteria of (28), these are stable points of operation as indicated in Fig. 6(b). Thus the tuning characteristics based on the second postulate of [8] contain multiple switching points between the $\lambda_g/2$ and λ_g modes of operation, while the stability criteria of (28) predict one mode-switching point around $L = 21$ mm corresponding to 12.4 GHz [Fig. 6(a)].

The tuning characteristics at -30-V varactor bias, corresponding to $C_V = 0.2$ pF, are shown in Fig. 7(a). The stable points of operation are arrived at by the second postulate of Eisenhart and Khan [8]. In the range $L = 8.2$–9.4 mm, though the susceptance condition of (27) is satisfied in two different frequency regions, there are no oscillation points as the load conductance $G_L(\omega)$ is greater than 5 mS and is too large for the device to drive. Also in the region $L = 10$–16 mm and up to frequencies slightly less than 14.8 GHz there are no oscillation points, as (27) is not satisfied. This results in a break in the $\lambda_g/2$ behavior. Corresponding load and device susceptance plots for this case are contained in Fig. 7(b). The stable points of operation obtained from the stability criteria of (28) are in very good agreement with those given by the second postulate of Eisenhart and Khan [8].

It is important to note that for $C_V = 0.2$ pF the tuning characteristic is mainly composed of a half-wavelength behavior pattern and a fixed-frequency oscillation pattern, the actual tuning characteristic consisting of regions of both these patterns connected by multiple switching points. Therefore, depending upon the stable point of operation, the theoretical model predicts either a very large or a negligibly small electronic-tuning range. The fixed-frequency operation, however, is of an intermittent nature and cannot be explained by simple package resonances and should not be confused with the so-called "frequency saturation" phenomena [8], [14]. It is of interest to note that the frequency of operation lies, in general, in the vicinity of the resonance point of the total susceptance appearing across the terminals 2–2′ of Fig. 5. But the intermittent nature of this oscillation and regions of no-circuit-controlled oscillations can only be explained by considering the equivalent circuit of the configuration in its entirety; that is, by the zero-susceptance condition of (27).

Discussion

A comparison of theoretical tuning characteristics with those obtained experimentally in a very limited range of short-circuit position ($L = 10$–14 mm) by Dean and Howes [4, fig. 8] shows that the proposed equivalent circuit does predict the performance at either end of the varactor bias in the correct manner. The important thing to notice is that for $C_V = 0.2$ pF the observed fixed frequency operation is predicted, where the simplified model proposed by Dean and Howes [4] had failed. It is also of interest to note that at $C_V = 0.2$ pF, corresponding to -30-V varactor bias voltage and $L \geq 14$ mm the authors had also observed stable oscillations at a lower frequency (< 15 GHz) [4, footnote 1 on p. 568] which their theoretical model had failed to predict. This oscillation frequency corresponds to the half-wavelength behavior and is correctly predicted by the equivalent circuit used here; the preferred mode of oscillation being determined by the stability condition.

However, the oscillation frequencies predicted by the theoretical model are generally lower than the experimental ones. This can be primarily attributed to package parameter values used in the equivalent circuit which may be at variance with actual values. The package equivalent-circuit representation has been a topic of much debate in recent years [15]–[17]. The actual package parameter values

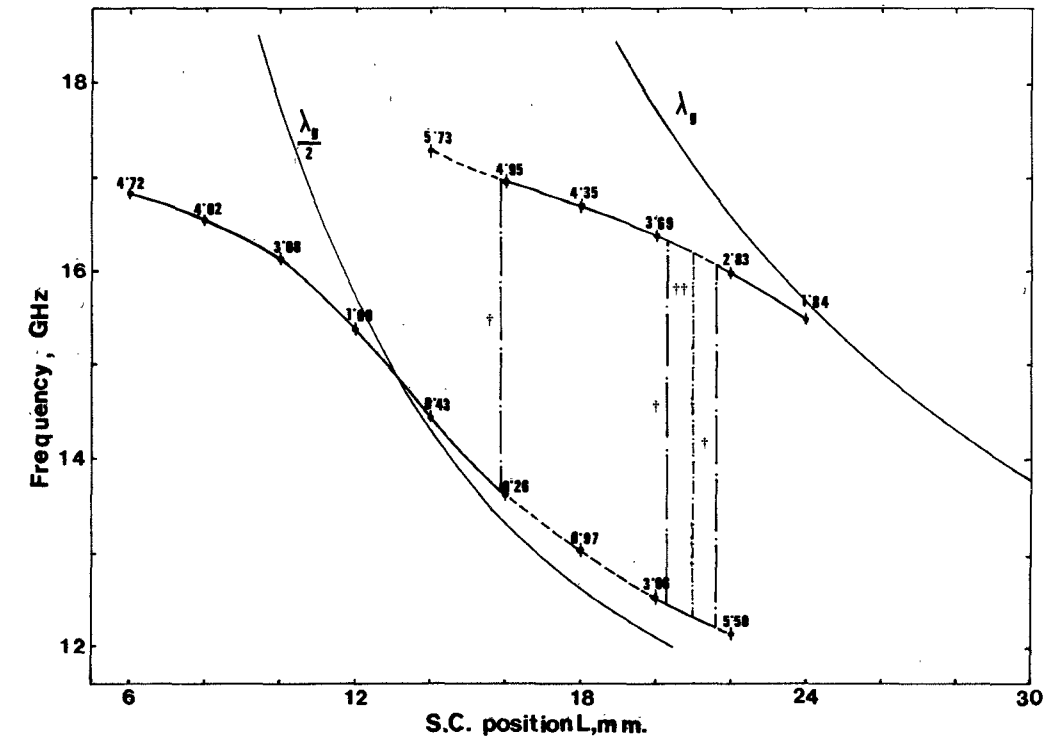

(a)

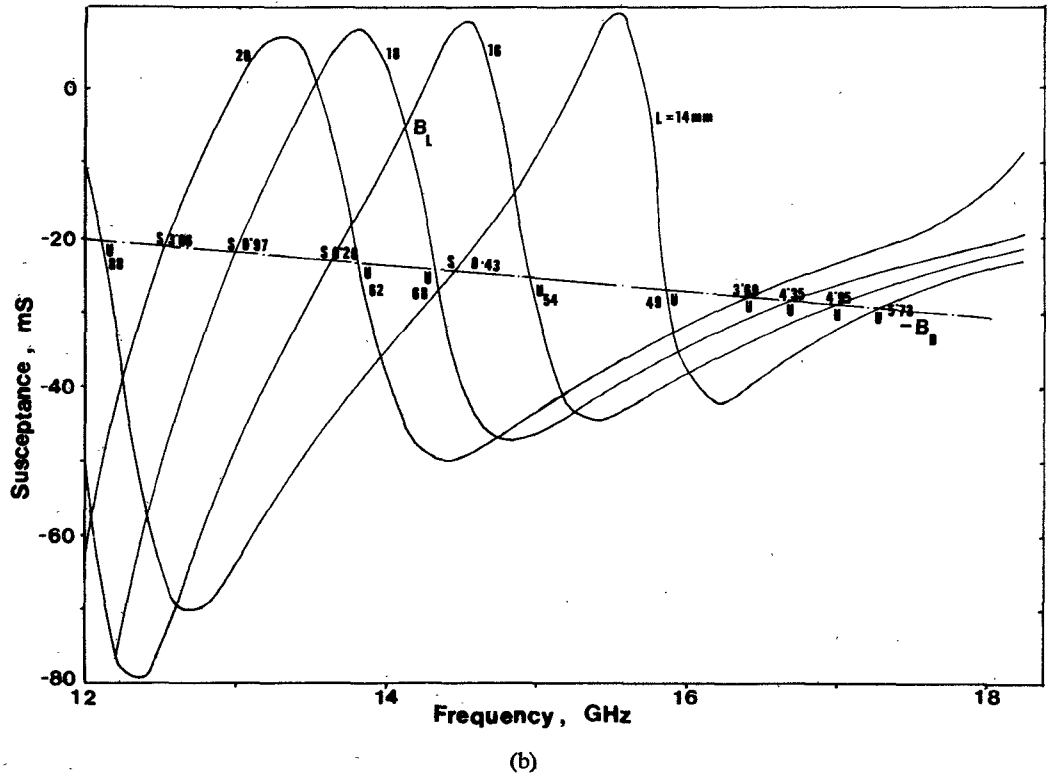

(b)

Fig. 6. (a) Theoretical tuning characteristics for the configuration of Fig. 1(a) for zero-biased varactor, $C_V(0) = 0.95$ pF. Parameter values as indicated in Fig. 5. Figures indicate load conductance G_L in millisiemens. †indicate switching between different modes according to postulate of [8]. ††indicate switching between different modes according to the stability criteria of (28). (b) Theoretical load and device susceptance variation with frequency for different short-circuit positions for the case of Fig. 6(a). Load conductance in millisiemens at each oscillation point is indicated. *S* and *U* denote stable and unstable oscillation points, respectively, based on the stability criteria.

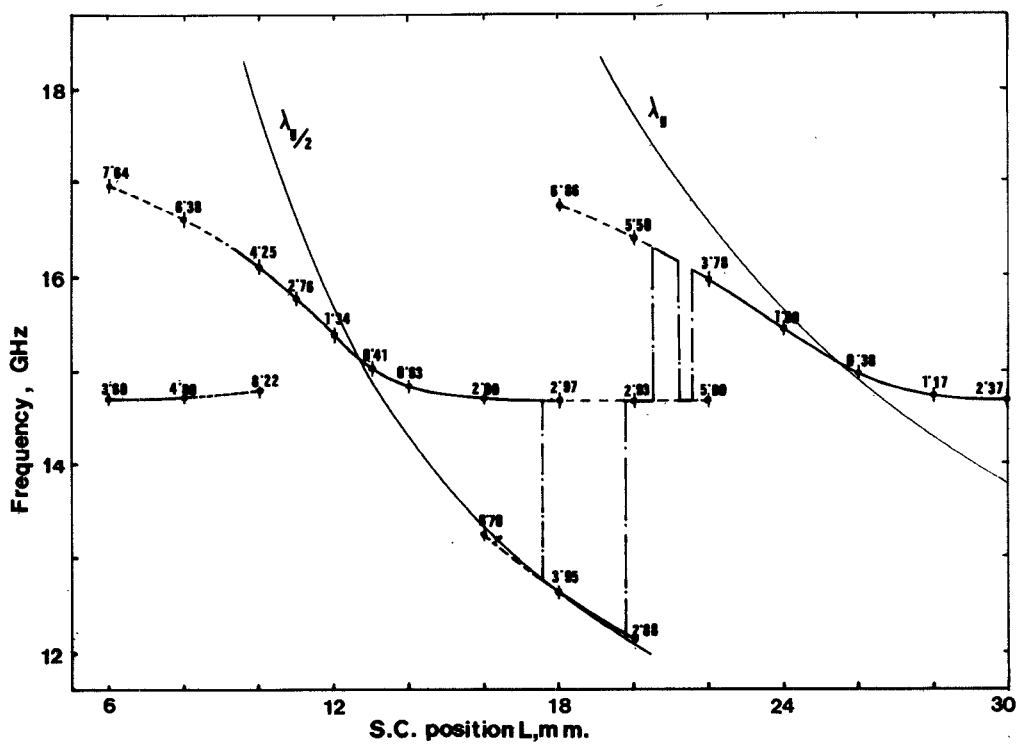

(a)

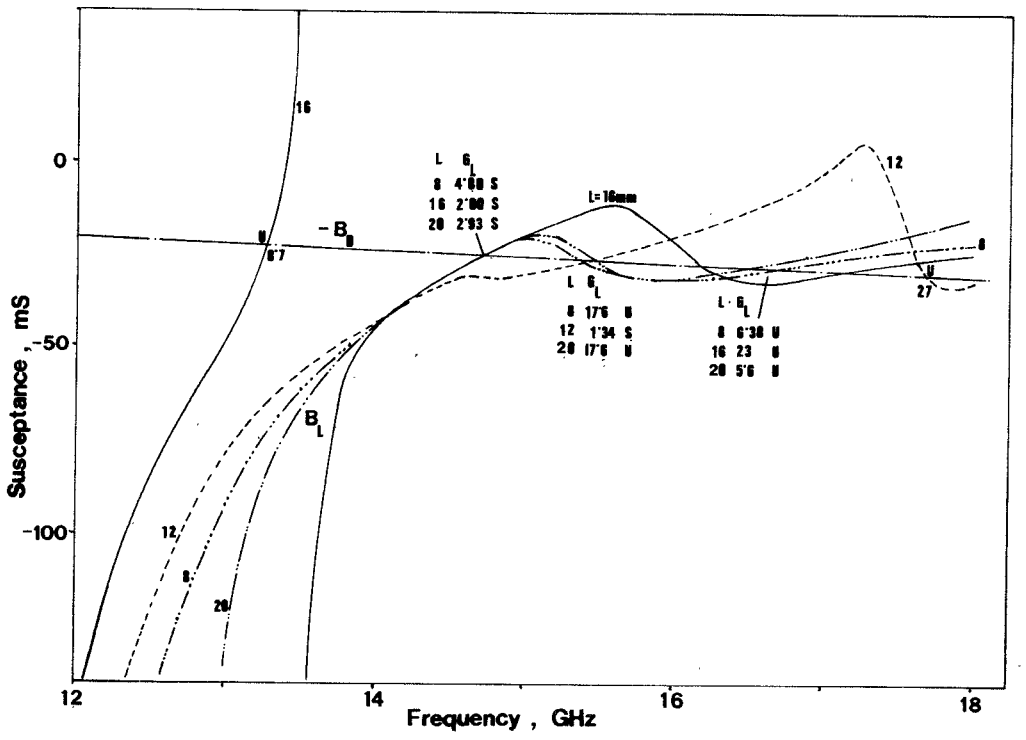

(b)

Fig. 7. (a) Theoretical tuning characteristics for the configuration of Fig. 1(a) for −30 V varactor bias, $C_V(30) = 0.2$ pF. Parameter values as indicated in Fig. 5. Figures indicate load conductance in millisiemens. Switching points between different modes are indicated according to the postulates of [8] and are in close agreement with those based on the stability criteria. (b) Theoretical load and device susceptance variation with frequency for different short-circuit positions for the case of Fig. 7(a). Load conductance in millisiemens at each oscillation point is indicated. *S* and *U* denote stable and unstable oscillation points, respectively, based on the stability criteria.

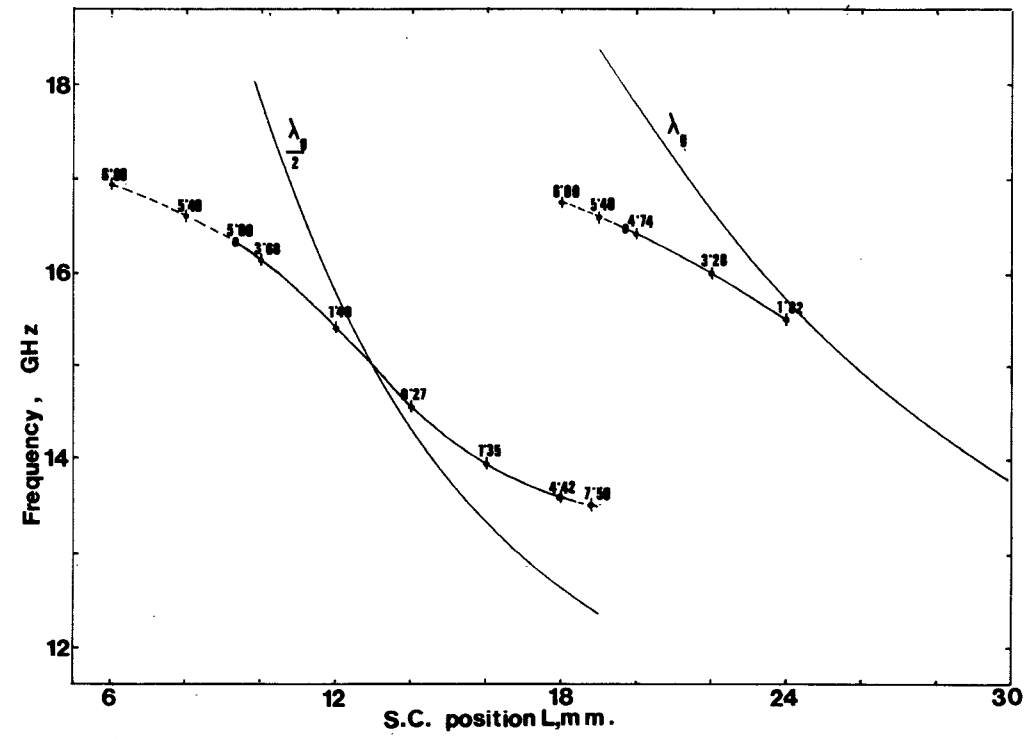

(a)

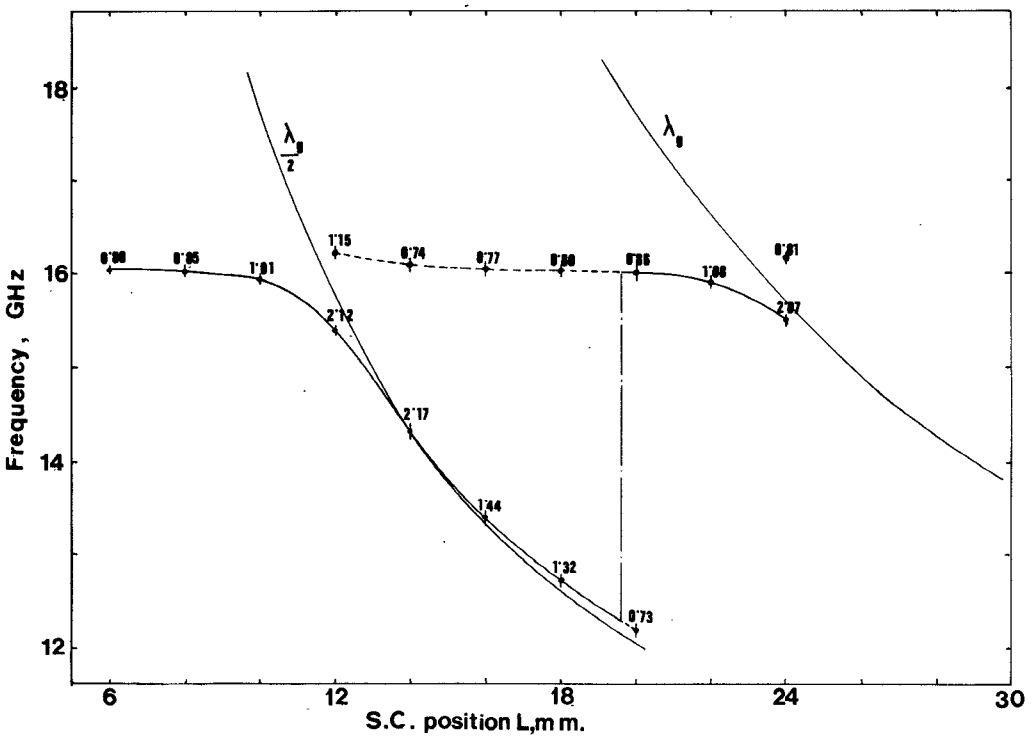

(b)

Fig. 8. Theoretical tuning characteristics for the configuration of Fig. 1(a) for (a) $C_V = 0.95$ pF and (b) $C_V(30) = 0.2$ pF. Parameter values are as shown in Fig. 5 except $L_{DV} = 0.6$ nH. Figures indicate load conductance in millisiemens.

play an important role in transforming the external impedance to the actual device terminals. This transformation is very critically dependent on package parameters at higher frequencies like K_u band and above, especially when the semiconductor device is in an S4 package.

In order to illustrate this dependence on package parameters, the varactor inductance was altered to 600 pH and tuning characteristics obtained as shown in Fig. 8(a) and (b). It can be seen that this slight change has radically altered the tuning characteristics. For $C_V = 0.95$ pF there are regions of no oscillation as the load conductance is too large for the device to drive. For $C_V = 0.2$ pF the fixed-frequency oscillation region has moved up to around 16.1 GHz and there are no forbidden regions of oscillation in

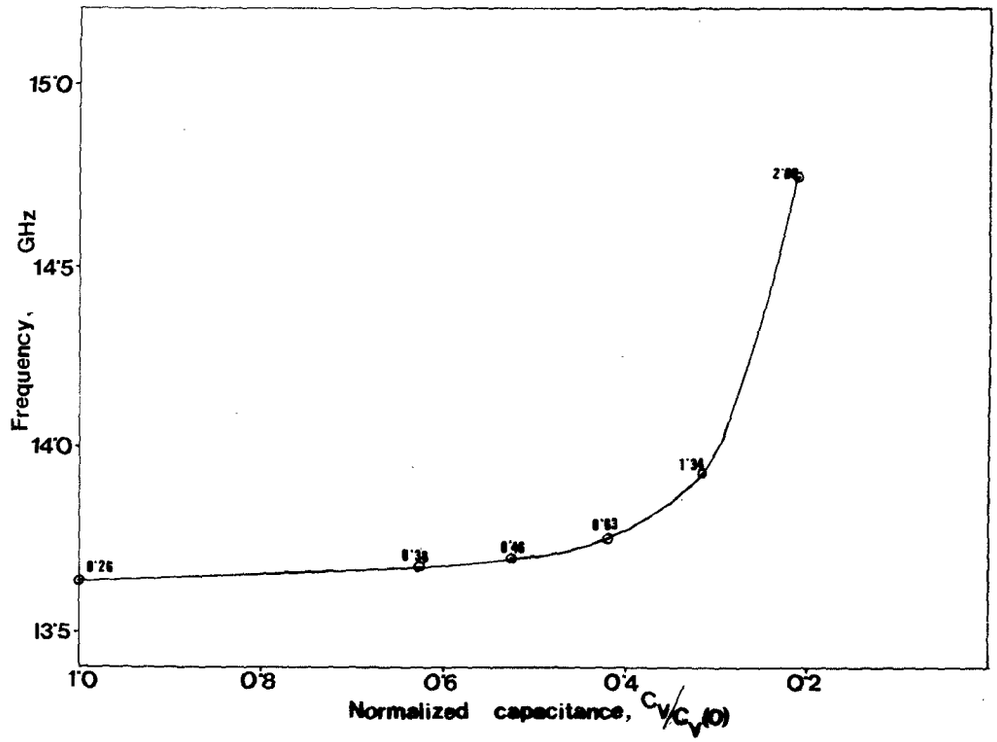

Fig. 9. Theoretical varactor-tuning characteristics for the configuration of Fig. 1(a) for the short-circuit position $L = 16$ mm. Parameter values are as in Fig. 5. Load conductance values in millisiemens are indicated.

which the zero-susceptance condition of (27) is not satisfied. As expected, the half-wavelength behavior is maintained in both cases.

Varactor-Tuning Characteristic

The varactor-tuning characteristics of the oscillator configuration can also be determined by the theoretical model. An examination of the tuning characteristics reveals that this will be very strongly dependent upon the short-circuit position L. Not only the amount and direction of the varactor tuning but also the stable points of the oscillation over the varactor-tuning range are determined by it.

In the practical case, however, the characteristics may be modified by the inherent hysteresis behavior of the transferred-electron-device oscillators. The actual varactor-tuning characteristics will depend upon the direction of the short-circuit travel, direction of varactor bias variation, and their interaction. It may also be affected by changes in the transferred-electron-device bias level. Fig. 9 indicates theoretical varactor-tuning characteristics for the case of Figs. 6 and 7 at $L = 16$ mm. The total tuning range is 1.1 GHz. It should be noted that no comparable experimental varactor-tuning characteristics are reported by Dean and Howes [3], [4].

Conclusions

This study has derived an equivalent-circuit representation for a single-post two-symmetrical-gap configuration, which can be used for the family of all such waveguide mounting configurations. Experimental work conducted on the post structure as an obstacle for the incident TE_{10} mode have shown excellent agreement with the theory.

Its application to a practical mounting arrangement has led to a successful explanation of the gross features experimentally observed, and which could not be explained by a simplified model. But for the strong dependence on the package parameters and lack of precise knowledge of other parameter values, the theoretical predictions could have been in better agreement with experimental results.

The nature of varactor-tuning characteristics obtainable with this configuration has been discussed and a theoretical characteristic indicated. It has been seen that the short-circuit position strongly influences the varactor-tuning behavior both in magnitude and nature.

References

[1] N. S. Chang, T. Hayamizu, and Y. Matsuo, "YIG tuned Gunn effect oscillator," *Proc. IEEE*, vol. 55, p. 1621, Sept. 1967.
[2] J. S. Joshi, "Wide-band varactor-tuned *X*-band Gunn oscillators in full-height waveguide cavity," *IEEE Trans. Microwave Theory Tech.*, vol. MTT-21, pp. 137–139, March 1973.
[3] M. Dean and M. Howes, "An electronically tuned Gunn oscillator circuit," *IEEE Trans. Electron Devices*, vol. ED-20, pp. 597–598, June 1973.
[4] ——, "Electronic tuning of stable transferred electron oscillators," *IEEE Trans. Electron Devices*, vol. ED-21, pp. 563–570, Sept. 1974.
[5] R. L. Eisenhart and P. J. Khan, "Theoretical and experimental analysis of a waveguide mounting structure," *IEEE Trans. Microwave Theory Tech.*, vol. MTT-19, pp. 706–719, Aug. 1971.
[6] O. L. El-Sayed, "Impedance characterization of a two-post mounting structure for varactor tuned Gunn oscillators," *IEEE Trans. Microwave Theory Tech.*, vol. MTT-22, pp. 769–776, Aug. 1974.
[7] N. Marcuvitz, *Waveguide Handbook* (M.I.T. Rad. Lab. Ser., vol. 10). New York: McGraw-Hill, 1951.
[8] R. L. Eisenhart and P. J. Khan, "Some tuning characteristics and oscillation conditions of a waveguide-mounted transferred electron diode oscillator," *IEEE Trans. Electron Devices*, vol. ED-19, pp. 1050–1055, Sept. 1972.

[9] W. A. Edson, *Vacuum Tube Oscillators*. New York: Wiley, 1953, pp. 430–450.
[10] K. Kurokawa, "Some basic characteristics of broad band negative resistance oscillator circuits," *Bell Systems Tech. J.*, pp. 1937–1955, July–Aug. 1969.
[11] W. C. Tsai, F. J. Rosenbaum, and L. A. MacKenzie, "Circuit analysis of waveguide cavity Gunn-effect oscillator," *IEEE Trans. Microwave Theory Tech.*, vol. MTT-18, pp. 808–817, Nov. 1970.
[12] C. P. Jethwa and R. L. Gunshor, "An analytical equivalent circuit representation for waveguide-mounted Gunn oscillators," *IEEE Trans. Microwave Theory Tech.*, vol. MTT-20, pp. 565–572, Sept. 1972.
[13] A. S. Templin and R. L. Gunshor, "Analytical model for varactor-tuned waveguide Gunn oscillators," *IEEE Trans. Microwave Theory Tech.*, vol. MTT-22, pp. 554–556, May 1974.
[14] B. C. Taylor, S. J. Fray, and S. E. Gibbs, "Frequency saturation effects in transferred electron oscillators," *IEEE Trans. Microwave Theory Tech.*, vol. MTT-18, pp. 799–807, Nov. 1970.
[15] W. J. Getsinger, "The packaged and mounted diode as a microwave circuit," *IEEE Trans. Microwave Theory Tech.*, vol. MTT-14, pp. 58–69, Feb. 1966.
[16] R. P. Owens and D. Cawsey, "Microwave equivalent circuit parameters of Gunn-effect-device packages," *IEEE Trans. Microwave Theory Tech.*, vol. MTT-18, pp. 790–798, Nov. 1970.
[17] R. P. Owens, "Mount-independent equivalent circuit of the S4 diode package," *Electronics Letters*, vol. 19, pp. 580–582, Sept. 23, 1971.

Integrated Approach to Microwave Design

JOHN W. BANDLER, SENIOR MEMBER, IEEE, PETER C. LIU, MEMBER, IEEE, AND HERMAN TROMP

Abstract—**A new, integrated approach to microwave design is presented involving concepts such as optimal design centering, optimal design tolerancing, optimal design tuning, parasitic effects, uncertainties in models and reference planes, and mismatched terminations. The approach is of the worst case type, and previously published design schemes fall out as particular cases of the ideas presented. The mathematical and computational complexity as well as the benefits realized by our approach is illustrated by transformer examples, including a realistic stripline circuit.**

I. Introduction

THE use of nonlinear programming techniques for the design of microwave circuits has been well established. Applications hitherto reported by the authors, for example, fall into two categories. 1) The improvement of a response in the presence of parasitics [1], [2], in which case the function to be minimized is of the error function type and the constraints, if any, are normally imposed on the design parameters. 2) Design centering and tolerance assignment to yield a minimum cost circuit that satisfies certain specifications, usually imposed on the frequency response, for all possible values of the actual parameters [3]. The function to be minimized is of the cost function type and the constraints are due to the specifications. Tuning elements may be introduced to further increase possible unrealistic tolerances and thus decrease the cost or make a circuit meet specifications [4].

No consideration, however, of optimal tolerancing or tuning of microwave circuits has been reported where parasitic effects were taken into account. A major complication is introduced here, since the models available for common parasitic elements normally include uncertainties on the value of the model parameters. These uncertainties are due to the fact that the model is usually only approximate and that approximations have to be made in the implementation of existing model formulas. A typical example of the latter is the relationship between the characteristic impedance and width of a symmetric stripline, where the formula involves elliptic integrals.

The model uncertainties can well be of the same order of magnitude as the tolerances on the physical network parameters so that a realistic design, including tolerances, can only be found when allowance is made for them. In the approach adopted, an attempt is made to deal with the model uncertainties in the same way as with the other tolerances. This involves, however, a complication in the formulation of the problem. The physical tolerances affect the physical parameters, whereas the model parameter uncertainties affect a set of intermediate parameters (which will be called the model parameters) in the calculation of the response.

In the present paper we consider design of microwave circuits with the following concepts treated as an integral part of the design process: optimal design centering, optimal design tolerancing, optimal design tuning, parasitic effects, uncertainties in the circuit modeling, and mismatches at the source and the load.

Manuscript received November 14, 1975; revised March 15, 1976. This work was supported by the National Research Council of Canada under Grant A7239 and by a Graduate Fellowship of the Rotary Foundation to one of the authors (H.T.). This paper is based on material presented at the 1975 IEEE International Microwave Symposium, Palo Alto, CA, May 12–14, 1975.

J. W. Bandler is with the Group on Simulation, Optimization, and Control and the Department of Electrical Engineering, McMaster University, Hamilton, Ont., Canada.

P. C. Liu was with the Group on Simulation, Optimization, and Control and the Department of Electrical Engineering, McMaster University, Hamilton, Ont., Canada. He is now with Bell-Northern Research, Verdun, P.Q., Canada.

H. Tromp was with the Group on Simulation, Optimization, and Control and the Department of Electrical Engineering, McMaster University, Hamilton, Ont., Canada. He is now with the Laboratory of Electromagnetism and Acoustics, University of Ghent, Ghent, Belgium.